NILES

Journal of Laser Science and Applications
journal homepage: https://jlsa.journals.ekb.eg

Cairo University

Corneal Ablation by 266-nm and 193-nm Lasers: A comprehensive Chemical Analysis Study Assisted with Machine Learning

Ibrahim Abdelhalim[a], Omnia Hamdy[a,*], Aziza Ahmed Hassan[b], Salwa Abdelkawi[c], Salah Hassab Elnaby[a] and

[a] Engineering Applications of Laser Department , National Institute of Laser Enhanced Sciences, Cairo University, Giza, 12613, Egypt.

[b] Medical Applications of Laser Department, National Institute of Laser Enhanced Sciences, Cairo University, , Giza, 12613, Egypt.

[c] Vision Science Department, Research Institute of Ophthalmology, Biophysics and Laser Science Unit, , Giza, Egypt

Abstract

Background: Laser-assisted in situ keratomileusis (LASIK) is a widely used refractive surgical procedure that typically involves the ablation of the corneal stroma using 193 nm excimer laser pulses. While this method is effective in reshaping the cornea, alternative laser sources such as nanosecond Q-switched solid-state lasers at 266 nm (fourth harmonic of Nd:YAG) offer potential benefits, particularly regarding their influence on the chemical integrity of ablated tissue.

Objective: This study aims to compare the chemical outcomes of corneal ablation using 193 nm excimer laser and 266 nm Qswitched laser pulses.

Methods: Using Fourier Transform Infrared (FTIR) spectroscopy, we investigate the molecular composition and bonding differences in the treated tissue. Additionally, machine learning algorithms are employed to support spectral analysis and enhance the interpretation of chemical changes induced by each laser source.

Results: The experimental FTIR results reveal distinct chemical differences between the two ablation techniques. Although the 266 nm Q-switched laser exhibits slightly lower ablation rates, it demonstrates favorable chemical effects on the tissue structure.

Conclusion: These findings, reinforced by machine learning analysis, contribute to a more comprehensive understanding of how laser parameters influence the biochemical outcomes of corneal ablation

Keywords: LASIK; Machine learning; corneal ablation; excimer laser; FTIR

I. Introduction

The cornea is the primary refractive element in the eye. It comprises five layers: the stroma, the Descemet membrane, the epithelium, Bowman's layer, and the endothelium [1]. The majority of the cornea's dry weight is made up of about two hundred layers of stroma which are primarily made of type I collagen fibrils [2]. Three amino acid chains that wind around one another to form a triple helix make up the unique structure of native collagen [3]. The primary components of the cornea are water and collagen. Collagen I, which makes up 78% of the corneal stroma, is the main type of collagen. Collagen III, IV, and V, as well as keratan sulfate and other trace amounts, make up around 7%. Proteoglycans are intricate molecules made of sugar chains and proteins that support the integrity of the cornea's moisture and clarity [4].

Collagen molecules can produce two different kinds of hydrogen bonds; the first kind is formed between the CAO or NOH groups that are between water molecules, and the other is developed between the NOH and CAO groups in neighboring chains to generate interchain hydrogen bonds [5]. According to X-ray diffraction assessments, bovine corneas contain at least 66% water [6]. The water molecules and the CAO and NOH groups in polypeptide chains exhibit two different kinds of hydrogen bonding. As a result, several kinds of hydrogen-bonded OOH peaks in the 3300–3600 cm^{-1} range of the IR spectrum can be expected [7]. Both the hydrogen-bound OOH stretching vibration and the nonhydrogen bonded (free) NOH stretching vibration (about 3450 cm^{-1}) are correlated with many peaks in the region of 3400 to 3600 cm^{-1}. The peak at 3316 cm^{-1} may represent the NOH stretching vibration. The nonhydrogen bonded (free) OOH stretching vibration band is represented by the strong peak at 3572 cm^{-1}. Additionally, vibrations of the carbonyl group (CAO) and typical amide I are detected at 1549 and 1651 cm^{-1} respectively [8].

By directing radiation in the infrared region that is absorbed by the sample, FTIR spectroscopy offers an appropriate method to investigate the structure of ocular proteins. Infrared absorption bands are unique to each sample.

Corresponding Author: Omnia Hamdy Email: omnia@niles.cu.edu.eg

Received April 4, 2025 Revised date: June 6, 2025 Accepted June 13, 2025

ISSN: 1687-8892

Amide I and Amide II are the most recognizable bands in the infrared spectra of corneal proteins and polypeptides [9].
FTIR can identify shifting distinctive absorption lines that are indicative of changes in protein structure. All nearby atoms and bonds are interacting to cause this shift. Quantum theory of molecular vibrations can be used to compute these shifts. Additionally, IR spectral datasets are widely available [10]. In the present study, we made use of a condensed set that has been published in Merck [11], [12]. Amide I, amide II, and amide III bands are the most prominent in the protein IR spectrum [9]. The amide I band (1600-1700 cm^{-1}) namely (1633.6, 1528, 1431.2, 1224, 1171.6, 1083.6 cm^{-1}) is caused by the carbonyl stretching vibration of the amide groups with some contribution from the C-N stretch. On the other hand, the amide II band (1510-1580 cm-1) specifically (1704, 1431, 1110, 1022 cm^{-1}) is sensitive to secondary structure conformation. While, Amide III (1200-1350 cm-1) namely (1602.8, 1501.6, 1180, 1050 cm-1) is a complicated band resulting from secondary structures [6].

These infrared bands are sensitive to hydrogen bonding, dipole–dipole interactions, and the peptide backbone geometry, making them well-established markers of the secondary structural change. Curve fitting identifies the amide I band, which is one of the secondary structure's primary components (helix at 1650-1658 cm^{-1} and sheet at 1620-1640 cm^{-1}). These bands have long been used to assess proteins' denaturation responses [13].

Recently, spectral identification has been found to be effectively aided by machine learning [14]. IR spectroscopy's primary purpose of delivering quick, preliminary information on molecules under study is well-aligned with the use of machine learning algorithms to aid in the interpretation of IR data. However, because of the greater complexity and variety of the vibrational spectra in these states, the model performs inferior on the infrared data acquired from organic molecules in the liquid and solid physical states. Furthermore, due to intermolecular interactions brought on by molecules' near proximity, vibrational spectra can be more complex in the liquid and solid phases [15].

In the present study, we aim to experimentally investigate and compare the chemical modifications in corneal tissue resulting from laser ablation using two distinct wavelengths; 193 nm excimer laser and the fourth harmonic of Nd:YAG 266 nm Q-switched solid-state laser. Building on earlier numerical predictions suggesting potential differences in post-ablation chemical composition, we employ Fourier Transform Infrared (FTIR) spectroscopy to analyze molecular alterations induced by each technique. Special attention is given to identifying variations in functional groups and bonding patterns within the treated tissue. To support a more refined interpretation of the spectral data, a machine learning model is applied, offering an advanced analytical approach to discern subtle chemical distinctions between the two methods. This comprehensive analysis seeks to bridge the gap between ablation efficiency and chemical outcome, contributing to a deeper understanding of how different laser sources influence the biochemical integrity of the cornea.

II. METHODS

A. Sample preparation

Ex-vivo rabbit eyes were purchased from a local butcher shop (Three rabbits, i.e. six corneas were employed) and transported to our lab in sterile containers within one hour after slaughter and transported in sterile containers filled with phosphate-buffered saline (PBS) to maintain hydration. To minimize variability, samples were held at 4°C on arrival and processed within 2 hours. Hydration levels were standardized by blotting surplus fluid using sterile filter paper prior to laser ablation. This methodology guarantees consistency in the O-H/N-H spectrum areas (3300-3600 cm^{-1}), as proven by pre-ablation FTIR baseline measurements. To assess the laser's ability to ablate the stroma, 7.5 mm of mechanical epithelial debridement was performed in the central region of the cornea. The samples were then exposed to 100 pulses of each laser type (i.e. 266 nm and 193 nm) at 20 distinct places. Consequently, the surface of the cornea was subjected to total 2000 laser pulses. Even though the overall pulse count of 2000 might seem excessive, it is consistent with modern LASIK procedures. Contemporary excimer lasers may produce more than 20,000 pulses in 20 seconds at frequency higher than 1000 Hz. For experimental precision, our pulse count represents a cautious estimate.

The excimer laser at 193-nm laser has a power of 1 mJ, spot size of 0.7 mm, and pulse duration of 4-7 ns. While, the Q-switched solid-state laser ((266 nm) has 1mJ power, 0.5 mm spot size, and 3-5 ns pulse duration. For the FTIR examination, the laser-ablated corneas were immediately inserted into liquid nitrogen (–196 ºC) to completely lyophilize them. After that, a Teflon hand homogenizer was used to dissolve the corneas into a powder to extract the proteins. Finally, potassium bromide (KBr) powder (98 mg KBr: 2 mg of powdered cornea) was combined with the acquired corneal powder to create the KBr disks. A Thermo Nicolet iS5 FTIR spectrometer (USA) was employed to obtain FTIR spectra in the 4000–1000 cm^{-1} range. The spectrometer was operated under continuous dry nitrogen gas and baseline adjusted.

B. Spectral Lines

The spectral peaks are detected at the local maxima of the curve. Additionally, there are kinks that indicate hidden maxima which are buried in the total spectra. To justify the set of collected lines, we reproduced the spectra assuming the lines are Gaussian function of wavenumber with an average line width of 30 cm^{-1} as can be seen in the theoretical study of [16]. For each line there is an amplitude *A(i)* where i=1, 2,.. , n, where n is the number of lines in the spectra. The measured value of the spectra at a spectral line *L(j)* is the sum of all Gaussian lines at that particular wavenumber *L* (j) so,

$$L(j) = \sum_{i=1}^{n} A(i)\exp\left(-\left(\frac{\nu_i - \nu_j}{30}\right)^2\right) \quad (1)$$

Accordingly, we get n equations in n variables that can be easily solved to get the values of *A(j)*. Using curve fitting we can justify all the set of spectral lines.

C. Spectral Analysis

Using the published databases [11], [16] we can assign a bond vibrational mode to each spectral line. Then, using the databases of functional groups, we can assign one or more

function group to each spectral line. To find more reliable assignment, the function group database sorted by functional groups (i.e. each function group has a finite number of several lines) has been used. Consequently, the functional groups which does not have all or most of the spectral lines were removed.

D. Machine Learning

A three-step technique was used to implement spectral processing in Python (version 3.9.7). The first part of the algortim finds spectral lines that are poorly resolved or overlapped. Closely spaced peaks are sometimes shown as a single wide line with inflections or kinks. The program uses the Least Squares Method (LSM) to deconvolute these composite lines, properly calculate the positions of individual spectral peaks, and create a comprehensive list of discovered lines. Gaussian deconvolution (scipy.optimize.curve_fit) with a 1.5% root-mean-square error tolerance was used to resolve overlapping peaks. In the second stage, the software uses the built-in spectral database of functional groups. It validates the previously identified spectral lines against this database. A functional group is considered present if all of its characteristic spectral lines can be recognized. This stage assures specificity while reducing false positives. all characteristic peaks had to be detected in order to identify functional groupings by stringent matching against a proprietary database (in JSON format). The third step calculates the relative abundance (weight) of each recognized functional group using the intensity of its characteristic peaks. A simulated spectrum is then generated, and the software iteratively adjusts the weights to reduce the difference between the reconstructed and measured spectra. Again, the divergence did not surpass 1.5%, demonstrating the model's robustness. The reconstructed spectra were verified against the original data, and relative abundances were computed using MinMax normalization of peak intensities. The steps of the implemented algorithm are summarized in the flowchart presented in Fig. 1.

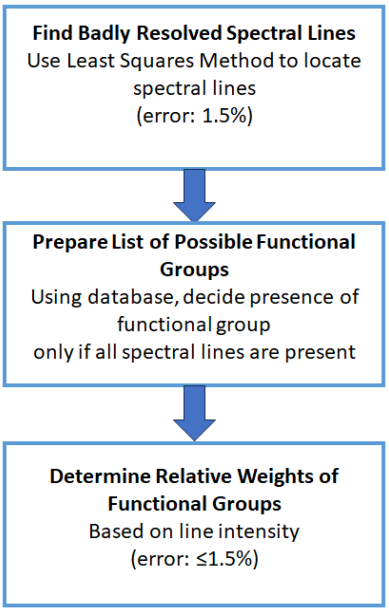

Fig. 1 Flowchart illustrating the main components of the proposed self-deciding algorithm for spectral analysis.

E. Statistical Analysis

A pairwise comparison weas carried out in order to evaluate any potentially notable variations in FTIR absorbance values between the experimental groups. Since there was no assumption of normality in the data distribution and the sample sizes were quite modest, non-parametric Mann-Whitney U tests were used for all comparisons [17]. Ordinal data or data that do not satisfy parametric assumptions, such those frequently seen in spectroscopic measurements, are appropriate for this strong statistical test. In particular, pairwise comparisons between Control and L193, Control and L266, and L193 and L266 were carried out. A predefined significance level (α) of 0.05 was used for all statistical analyses. All statistical calculations were carried out using Python (version 3.9.7), utilizing well-known libraries including SciPy for specialized statistical functions and NumPy for numerical operations.

III. RESULTS

The measured spectra of the control tissue (i.e. un-irradiated cornea), the tissue remaining after ablation by excimer laser at 193 nm, and the tissue remaining after ablation by fourth harmonic of Nd-YAG laser at 266 nm is presented in Fig. 2

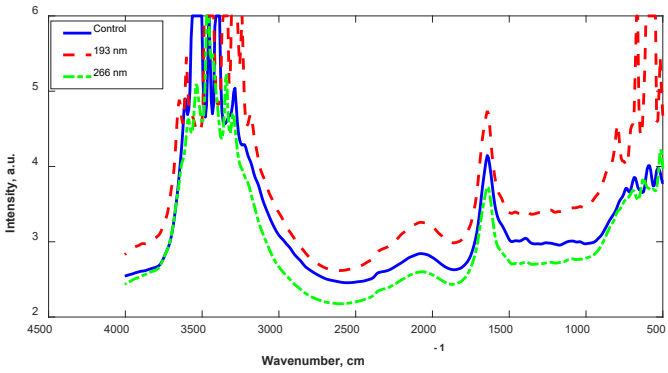

Fig. 2 Originally measured FTIR spectra. Control is solid line, ablated by excimer dashed line and ablated by fourth harmonic of Nd-YAG is represented by dash point line.

Some peaks of the spectra were limited to absorption value of 6. To be able to study the spectra mathematically we used a curve fitting program to complete the spectra. The corrected spectra is shown in Fig. 3

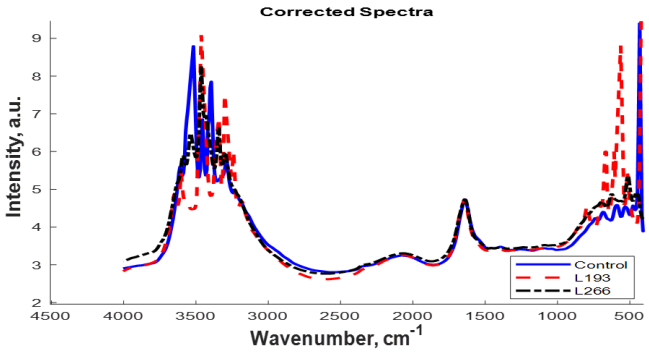

Fig. 3 The reproduced FTIR spectra after utilizing curve fitting.

A well-known method to identify spectral lines in a measured spectrum is to differentiate the spectrum. The 1st derivative of the spectrum will find the exact position of local maxima. To complete the finding we must use the second derivative to find other lines that produce kinks in the spectrum. Using a proprietary algorithm for identification of spectral lines and their strength we get about 70 lines in the region 400-4000 cm^{-1}. Many of these lines cannot be identified by simple observations. With human help can produce a closer identification of the spectral lines which when added should reproduce the measured spectrum. Since the spectra had very smooth intervals, we divided the spectra into 3 regions 500 – 1030 cm^{-1}, 1380 – 1700 cm^{-1}, and 3170 – 4000 cm^{-1}. We concentrate on these ranges. Using the above-mentioned methods, we could determine 70 of the important spectral lines and their corresponding strengths. Seventy spectral lines were resolved by the proposed algorithm (compared to fifty-two manually detected), including buried peaks in Amide I/II areas (Fig. 2). The functional group designations matched published collagen spectra 100 percent of the time [13], and simulated spectra replicated experimental data 98.5% of the time (MSE =.0015). By imposing physical limitations (e.g., fixed linewidths, stringent group rules), our deterministic method provides great precision with limited data, in contrast to CNNs that require massive training sets [14]. For corneal FTIR, where sample sizes are tiny and peak overlaps are frequent, this is crucial.

IV. RESULTS

The most characteristic bands found in the infrared spectra of corneal proteins and polypeptides are Amide I and Amide II. These ascend from the amide bonds that link the amino acids. The absorption related to the Amide I band leads to stretching vibrations of the C = O bond of the amide, and absorption related to the Amide II band leads primarily to bending vibrations of the N–H bond. Both C = O and the N–H bonds are involved in the hydrogen bonding between these two different elements of the secondary structure.

Published work for FTIR spectrum interpretation with the help of machine learning algorithms dealt with Convolutional Neural Networks as assignment problems. We shall adopt another technique based on minimizing a loss function for each group. The loss function is calculated as the sum of differences between the values mentioned in the databases and that present in the spectra. We used this approach to treat the spectral shift that may happen due to the spectrometer (constant shift error) and the shift of peaks due to interactions of other atoms in the molecular structure (variable shift error). We used Python algorithms for identification of functional groups.

We observed there are common lines in all spectra. These are bonds that have been preserved from the original stroma after ablation by either the 193 nm laser or the 266 nm. These correspond to unchanged structures. There are 29 out of total 70 identified lines as shown in Table 1. In all tables there are lines that can be assigned to more than one bond due to overlapping. We used the machine learning algorithms to identify functional groups as in the next section. Mainly the broad band at ~2100 cm^{-1} and the band at 1650 cm^{-1} conserve their strength, some O-H stretching and N-H of primary amine are left unchanged as in the table. Peak assignments for overlapping bands (e.g., 1650 cm^{-1} for Amide I vs. C=C) were cross-referenced with the Merck FTIR database [11] and validated against Baronio & Barth (2020) [13], which provides DFT-calculated vibrational modes for collagen. In the following we use the abbreviation L193 (cornea ablated by laser at wavelength 193nm), L266 (cornea ablated by laser at wavelength 266nm) and Control for the untreated cornea.

Table 1 Lines in common in the control, ablated by 193 nm laser and by the fourth harmonic of Nd:YAG (266 nm)

CONTROL		**L193**		**L266**		**Bond**	**Compound**	**Bond**	**Compound**
CM^{-1}	VAL	CM^{-1}	VAL	CM^{-1}	VAL				
3934.1	2.5	3926.4	2.7	3934.1	3.1				
3733.5	3.3	3748.9	3.1	3741.2	3.6				
3610.1	5.4	3602.4	5.0	3633.2	4.2	O-H stretch	alcohol		
3540.7	3.0	3548.4	3.8	3533.0	6.4	N-H stretch	Amine	O-H stretch	Alcohol
3448.1	5.3	3463.5	7.7	3455.8	6.7	O-H stretch	Alcohol		
3417.2	4.2	3425.0	5.2	3425.0	4.3	N-H	Amine	O-H stretch	Alcohol
3386.4	5.9	3371.0	5.4	3394.1	4.9	N-H	primary Amine	O-H stretch	Alcohol
3324.7	5.1	3332.4	4.2	3340.1	6.3	N-H	primary Amine	N-H	Amine
3278.4	5.3	3270.7	3.6	3286.1	3.7	C-H	Alkene	O-H stretch	Alcohol
3216.7	4.7	3239.8	5.2	3232.1	4.8	O-H stretch	Carboxylic Acid	O-H stretch	Alcohol
3124.1	4.0	3139.5	3.7	3155.0	3.6	O-H stretch	Carboxylic Acid		

3070.1	3.8	3085.5	3.7	3070.1	3.7	O-H stretch	Carboxylic Acid		
2962.1	3.3	2962.1	3.2	2923.6	3.2	C-H stretch	Alkene	O-H	Acid
2854.1	3.1	2838.7	2.9	2854.1	3.0	C-H stretch	Alkene	O-H	Acid
2645.9	2.3	2653.6	2.6	2645.9	2.8	O-H	Acid		
2615.0	2.3	2545.6	2.6	2553.3	2.8	O-H	Acid		
2414.4	2.8	2422.2	2.7	2429.9	2.9				
2321.9	2.1	2321.9	2.9	2314.2	2.5				
2221.6	3.1	2260.2	3.0	2244.7	3.0	C N trible	Nitrile		
2136.7	3.2	2183.0	3.1	2198.5	3.1	C C trible	Alkene		
2075.0	3.2	2067.3	3.0	2067.3	3.3	C C trible	Alkene		
1974.8	2.9	1982.5	3.1	1951.6	3.2	C C trible	Alkene		
1666.2	3.3	1666.2	4.0	1643.1	3.5	C=C	Alkene	Amide	
1612.2	3.7	1627.6	3.9	1619.9	3.0	C=C	Alkene		
1450.2	3.4	1450.2	2.8	1450.2	3.4	C-H bending	Alkane		
1380.8	2.1	1380.8	3.2	1388.5	2.1	C-H bending	Alkane		
1249.6	2.9	1295.9	3.3	1234.2	2.1	C-N	Amine,Amide		
1218.8	2.1	1218.8	2.5	1218.8	2.0	C-N	Amine,Amide	C-O	Alcohols
1187.9	2.9	1180.2	3.2	1164.8	3.4	C-N	Amine,Amide	C-O	Alcohols
771.4	3.7	786.8	4.1	786.8	4.2	C-H bending	1,2,4-trisubstituted		
732.8	3.8	748.2	3.5	732.8	4.1	C-H bending	1,2,4-trisubstituted		
686.5	3.3	702.0	3.9	694.2	4.3	C-H bending	1,2,4-trisubstituted		
671.1	1.2	663.4	5.6	678.8	4.6				
516.8	2.5	516.8	5.4	509.1	5.2				
470.5	3.6	470.5	4.0	455.1	3.6				

In addition to data presented on Table 1, there were 10 lines in common between the control and stroma ablated by 193nm laser as shown in Table 2, while in the case of ablation by the fourth harmonic of Nd:YAG (266 nm) there are 12 lines left unchanged as shown in Table 3. This increases the resemblance of these tissues with the control vis-à-vis that ablated by 193 nm laser.

Table 2 Common lines between control tissue and that ablated by 193 nm laser.

CONTROL		**L193**		**Bond**	**Compound**	**Bond**	**Compound**
CM-1	VAL	CM-1	VAL				
3826.1	3.0	3887.8	2.6				
3517.5	5.4	3517.5	3.1	N-H stretch	Amine	O-H stretch	alcohol
3502.1	2.8	3486.7	2.0	N-H stretch	Amine	O-H stretch	alcohol
3170.4	4.2	3170.4	1.2	O-H stretch	Carboxylic Acid		
2915.8	3.2	2900.4	3.0	C-H stretch	Alkene	O-H	Acid
2738.4	2.9	2761.6	2.7	O-H	Acid		
2476.2	2.8	2491.6	2.6				
2013.3	2.9	2028.7	2.9	C C trible	Alkyne		
1643.1	2.5	1643.1	0.4	C=C	Alkene	Amide	

1396.2	2.0	1419.4	2.5	C-H bending	Alkane

Table 3 Lines in common in the control cornea, and by fourth harmonic of Nd:YAG (266 nm).

CONTROL		**L266**		**Bond**	**Compound**	**Bond**	**Compound**
CM-1	VAL	CM-^{1}	VAL				
3995.8	2.1	3988.1	3.1				
3895.5	2.7	3880.1	3.2				
3563.8	5.2	3586.9	5.7	O-H stretch	Alcohol		
2345.0	2.1	2345.0	2.5				
1519.6	3.6	1511.9	3.2	N-O			
1311.4	3.4	1311.4	3.4				
1079.9	3.3	1079.9	3.2	C-N	Amine, Amide	C-O	Alcohols
1041.4	1.7	1041.4	3.2	C-N	Amine, Amide	C-O	Alcohols
979.7	3.3	979.7	3.5	C=C bending	Alkene		
833.1	3.7	833.1	4.0	C-H bending	1,2,4-trisubstituted		
578.5	4.4	586.3	2.9				
432.0	9.1	432.0	3.1				

Additionally, there were 5 lines appear only in tissues ablated by 193 nm as summarized in Table 4

Table 4 Spectral lines in tissues ablated by 193 nm

L193		**Bond**	**Compound**
CM-1	VAL		
3849.2	1.8		
3702.7	3.6	O-H stretch	alcohol
3031.6	3.5	C-H stretch	Alkene
1920.8	3.0	C C trible	Alkene
1249.6	2.8	O-H bending	phenol

The line 3895.5 cm^{-1} was shifted in the case of L193 to 3849.2 cm^{-1}, which indicates changes in the structure and position of bond. There are new O-H and C-H stretching lines, and triple C bonds. On the other hand, L266 produces only 2 spectral lines that didn't exist in the other spectra as shown in Table 5.

Table 5 Spectral lines in tissues ablated by 266 nm

L266		Bond	Compound
CM-1	VAL		
1835.9	3.1		
1373.1	2.0	C-H bending	alkane

The new spectral lines that appear in L266 are few and lie in the fingerprint region. However, there were new 7 lines are common in L266 and L193 Table 6

There are 7 new lines that didn't exist in the control spectra indicate new O-H stretching due to alcohol bonds and Nitrogen bonds. There were 6 lines absent from L266 and L193. Meaning they are broken bonds. Table 7 presents the line at 3518 in the control which is completely absent in L193 which means this bond is selectively broken by the excimer laser.

Each function group has several characteristic lines. Although a spectral line can be due to more than one function group. However, we need to look to the function group as a hole, that is if not all the lines are present, we reject that group, only if all the lines are present, we identify that group. The problem is not that easy due to shifting the spectral lines. A loss function is used for each group where the optimization program of Python is used. The functional groups can be shown in Fig. 4.

Changes in chemical composition may not be assisted easily, but changes in bonds can indicate that C=C bond does not change. N-H bond is reduced and changed from Amine groups into Alkyne groups. In the same time O-H groups are also reduced. Moreover, the missed C–H ring band was restricted. In line with other histological investigations, the preservation of N-H bonds in L266-treated tissue indicates less protein denaturation [18]. These results agree with previous study that conducted on adult four months hyperoxia mice which may prove that LED laser exposure may lead to an improvement in the membrane structure of retinal cells [19]. Changes in phosphate group (symPO2) and amide I seem to relate to spatial changes in the positions of the phosphate groups in the protein helix. Therefore, it probably reveals initial changes in the secondary and tertiary structure of the protein also may cause changes in genetic materials [20].

The quantitative investigation of the FTIR absorbance spectra revealed vital information about the distinct impacts of L193 and L266 laser treatments on the molecular makeup of the samples. The statistically significant variations in O-H stretch intensities reported for the L193 group compared to controls ($p=0.013$) indicate that the L193 laser causes a more pronounced disturbance of hydrogen bonding networks, water content, and hydroxyl functional groups. In contrast, while the

L266 application produced a significant change, it was limited to the N-H stretch intensities when compared to controls (p=0.021). This unique spectral response suggests that, while the L266 laser affects the N-H bond environment, it may have a less ubiquitous effect on the overall molecule structure than the L193.

Table 6 Common spectral lines in L266 and L193

L193		L266		Bond	Compound	Bond	Compound
CM-1	VAL	CM-1	VAL				
3826.1	2.2	3826.1	3.3				
3640.9	4.3	3664.1	3.6	O-H stretch	alcohol		
3301.5	5.8	3301.5	2.9	C-H	Alkene	O-H stretch	Alcohol
3185.8	3.7	3185.8	3.7	O-H stretch	Carboxylic Acid		
2121.3	3.2	2136.7	3.3	N=C=N	carbodiimide		
1542.8	3.5	1550.5	3.3	N-O			
609.4	5.6	617.1	4.2				

Table 7 Spectral lines in control samples

CONTROL		Bond	Compound	Bond	Compound
CM-1	VAL				
3972.6	1.8				
3394	7.8	N-H	Amine		
1025.9	2.1	C-N	Amine, Amide	C-O	Alcohols
918.0	3.2	C=C bending	alkene		
879.4	3.2	C=C bending	alkene		
640.3	3.8				
532.3	2.7				

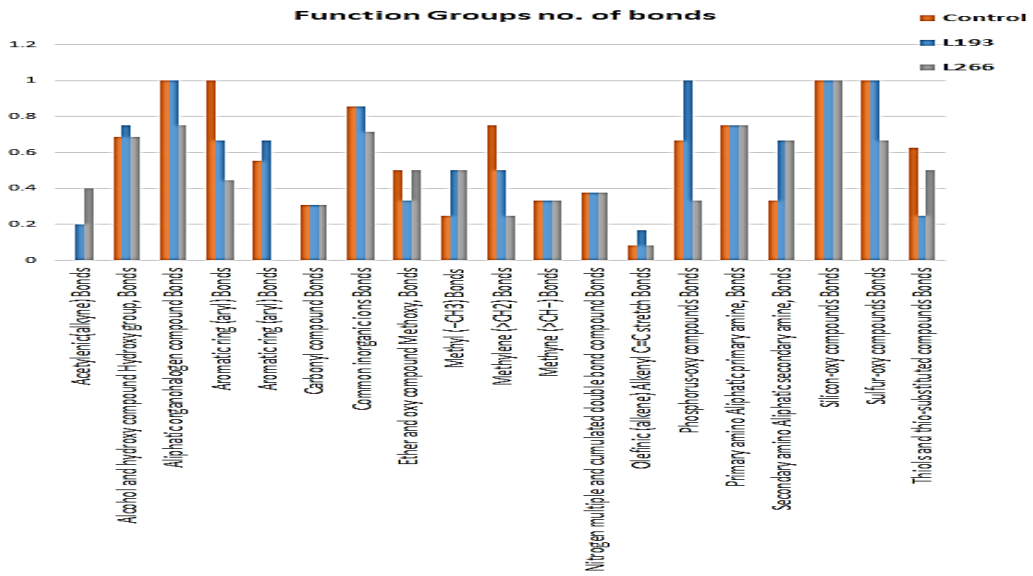

Fig. 4 Detailed Functional Groups Estimation

We further used algorithms to concise and reduce the data as shown in Fig. 5

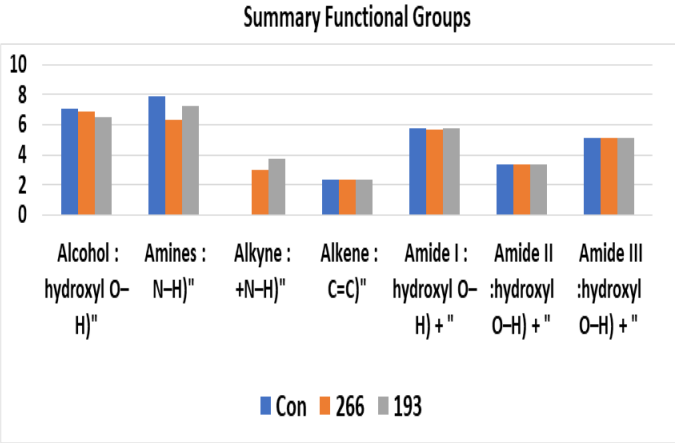

Fig. 5 Reduced list of functional groups.

V. CONCLUSION

There are significant differences between the control, L193, and L266 spectra. Some bonds were missing after the ablation. Other bonds are shifted indicating structural changes. New lines appear at 3340 indicating the presence of secondary amine. L193 produces new 3649, 3240, and 3186 cm-1 which correspond to carboxyl. When using the hole spectra, we find that L266 spectra is correlated to the control at 90%, while the L193 is correlated much less at 70%. Indicating that the changes after exposure to laser 266nm is very near to the control tissue. The implications of these findings are significant for the field of refractive surgery. Understanding the chemical modifications resulting from different laser ablation methods can inform the development of improved techniques for corneal reshaping and vision correction. By elucidating the chemical perspective of corneal ablation, this study contributes to the broader understanding of laser-tissue interactions and furthers the advancement of laser-based surgical procedures.

Conflict of interest: None
Funding: Not Applicable

REFERENCES

1. Willoughby CE, Ponzin D, Ferrari S, Lobo A, Landau K, Omidi Y. Anatomy and physiology of the human eye: effects of mucopolysaccharidoses disease on structure and function–a review. Clin Exp Ophthalmol. 2010;38:2–11. doi:10.1111/j.1442-9071.2010.02363.x.
2. Almubrad T, Akhtar S. Structure of corneal layers, collagen fibrils, and proteoglycans of tree shrew cornea. Mol Vis. 2011;17:2283–91.
3. Antonio JDS, Jacenko O, Fertala A, Orgel JP. Collagen structure-function mapping informs applications for regenerative medicine. Bioengineering. 2021;8(3):1–23. doi:10.3390/bioengineering8010003.
4. Espana EM, Birk DE. Composition, structure and function of the corneal stroma. Exp Eye Res. 2020;198:1–47. doi:10.1016/j.exer.2020.108137.
5. Fu I, Case DA, Baum J. Dynamic water-mediated hydrogen bonding in a collagen model peptide. Biochemistry. 2015;54(39):6029–37. doi:10.1021/acs.biochem.5b00622.Dynamic.
6. Jayasuriya AC, Scheinbeim JI, Lubkin V, Bennett G, Kramer P. Piezoelectric and mechanical properties in bovine cornea. J Biomed Mater Res - Part A. 2003;66(2):260–5. doi:10.1002/jbm.a.10536.
7. Ikemoto Y, Kato Y, Morikawa K, Taniguchi K, Miyamoto A, Yamamoto T. Infrared Spectra and Hydrogen-Bond Configurations of Water Molecules at the Interface of Water-Insoluble Polymers under Humidified Conditions. J Phys Chem B. 2022;126(22):4143–51. doi:10.1021/acs.jpcb.2c01702.
8. Dai F, Zhuang Q, Huang G, Deng H, Zhang X. Infrared Spectrum Characteristics and Quantification of OH Groups in Coal. ACS Omega. 2023;8(19):17064–76. doi:10.1021/acsomega.3c01336.
9. Kong J, Yu S. Fourier transform infrared spectroscopic analysis of protein secondary structures. Acta Biochim Biophys Sin (Shanghai). 2007;39(8):549–59. doi:10.1111/j.1745-7270.2007.00320.x.
10. Tanabe K, Oto TMA, Ura TTAM, et al. Identification of Chemical Structures from Infrared Spectra. Appl Spectrosc. 2001;55(10):1394–1.
11. Sigma-Aldrich. Photometry and Reflectometry [Internet]. [cited 2025 Jun 13]. Available from: https://www.sigmaaldrich.com/EG/en/applications/analytical-chemistry/photometry-and-reflectometry
12. Punjabi D, Kaur A, Bhatia K, Singh K, Singh B, Singh A, et al. Infrared spectrum analysis of organic molecules with neural networks using standard reference data sets in combination with real-world data. J Cheminform. 2025;17(24):1–13. doi:10.1186/s13321-025-00960-2.
13. Baronio CM, Barth A. The Amide i Spectrum of Proteins - Optimization of Transition Dipole Coupling Parameters Using Density Functional Theory Calculations. J Phys Chem B. 2020;124(9):1703–14. doi:10.1021/acs.jpcb.9b11793.
14. North NM, Enders AA, Cable ML, Allen HC. Array-Based Machine Learning for Functional Group Detection in Electron Ionization Mass Spectrometry. ACS Omega. 2023;8(27):24341–50. doi:10.1021/acsomega.3c01684.
15. Krzyżanowski M, Matyszczak G. Machine learning prediction of organic moieties from the IR spectra, enhanced by additionally using the derivative IR data. Chem Pap. 2024. doi:10.1007/s11696-024-03301-z.
16. Mistry BD. Handbook of Spectroscopic Data Chemistry. Jaipur, India: Oxford Book Company; 2009.
17. Sainani KL. Dealing With Non-normal Data. PM&R. 2012;4(12):1001–5. doi:10.1016/j.pmrj.2012.10.013.
18. Abdelkawi SA, Hassan AA. Evaluation of protein change and oxidative stress index after photodynamic therapy of

corneal neovascularization. Gen Physiol Biophys. 2012;31:449–55. doi:10.4149/gpb.
19. Sabry M, Abdelkawi S, El Saeid A, El Rashedi A. Low level laser therapy for hyperoxia-induced retinal protein deformations evaluated by FTIR study. Egypt J Biomed Eng Biophys. 2020;21(1):87–96. doi:10.21608/ejbbe.2020.41564.1036.
20. Albarracin R, Natoli R, Rutar M, Valter K, Provis J. 670 nm light mitigates oxygen-induced degeneration in C57BL / 6J mouse retina. BMC Neurosci. 2013;14(125):1–14.